Supplementary Information

An Artificial Photosynthetic System with CO_2-Reducing Solar-to-Fuel Efficiency Exceeding 20%

Yanjun Xiao‡ [a], Yao Qian‡ [a], Anqi Chen [a], Tian Qin [a], Fan Zhang [a], Hehua Tang [a], Zetian Qiu [a], Bo-Lin Lin*[a]

[a]School of Physical Science and Technology, ShanghaiTech University, Shanghai 201210, China.

‡These authors contributed equally to this work.
*Correspondence to: linbl@shanghaitech.edu.cn

.

This PDF file includes:

Experimental section
Figs. S1 to S12
Tables S1 to S5

References

Experimental section

The detailed derivation for the STF efficiency:

For a common PV-EC system, it usually contains three parts: the PV device as a solar energy input, an electrochemical system for electric energy conversion and storing in chemical energy, and a coupling system which matches the electrical output (current and voltage) of the PV device to the electrical input of the EC process. In this arrangement, the steady-state efficiency η_{STF} with which solar power is transferred to chemical fuels is given by

$$\eta_{STF} = \eta_{PV} \cdot \eta_{EC} \cdot \eta_C \quad \text{Eq. (S1)}$$

where η_{PV}, η_{EC}, and η_C are the efficiencies of the PV device, the EC process, and the coupling arrangement, respectively (Winkler, M. T. et al. P Natl Acad Sci USA 110, E1076-E1082, doi:10.1073/pnas.1301532110 (2013)).

The efficiency η_{PV} of a solar cell is

$$\eta_{PV} = \frac{FF \cdot V_{OC} \cdot J_{SC}}{P_{solar}} \cdot 100\% \quad \text{Eq. (S2)}$$

(Especially, when N identical solar cells are connected in series, their output voltages sum up to the overall voltage while the current density decreases to 1/N.)

The electric energy efficiency η_{EC} of an electrochemical process is generally dominated by kinetic limitations rather than thermodynamic ones. The operating voltage (V_{op}) must exceed the thermodynamic potential (μ_{th}) to achieve a sufficient reaction rate or operating current density (J_{op}). For a fuel-generating reaction, the power flow into the stored specific chemical energy is (μ_{th}*J_{op}*FE), whereas the total electrical energy dissipated is (V_{op}*J_{op}). Thus, the electric energy efficiency of the electrochemical reaction is

$$\eta_{EC} = \frac{\mu_{th} \cdot FE}{V_{op}} \quad \text{Eq. (S3)}$$

The efficiency η_C of the coupling system is entirely dependent on the choice of implementation, and its efficiency is not limited by any fundamental consideration. In principle, the simplest way to couple the systems may be to perform the anodic and cathodic reactions on the positive and negative terminals of a buried junction (or series of solar cells), respectively (just like what we have done in our work). Such a direct electrical connection is equivalent to constraining the currents and voltages of the PV device and the EC system to be identical: $I_{solar} = I_{EC}$ and $V_{solar} = V_{EC}$. Graphically, this constraint identifies the operational state of the coupled PV-EC device as the point at which the steady-state current–voltage properties of the PV device and the EC system intersect. Referring to Eq. 3, the coupling efficiency is

$$\eta_C = \frac{V_{op} \cdot I_{op}}{FF \cdot V_{OC} \cdot I_{SC}} = \frac{V_{op} \cdot J_{solar}}{FF \cdot V_{OC} \cdot J_{SC}} \cdot 100\% \quad \text{Eq. (S4)}$$

Using the above expressions, Eq. 2 can be rewritten as

$$\eta_{STF} = \frac{FF \cdot V_{OC} \cdot J_{SC}}{P_{solar}} \cdot \frac{\mu_{th} \cdot FE}{V_{op}} \cdot \frac{V_{op} \cdot J_{solar}}{FF \cdot V_{OC} \cdot J_{SC}} = \frac{\mu_{th} \cdot FE \cdot J_{solar}}{P_{solar}} \cdot 100\% \quad \text{Eq. (S5)}$$

The final term of Eq. 5 represents the STF efficiency of any one electrochemical reaction driven by solar power. And for any PV-EC system with a specific CO_2RR, the Eq.5 can be rewritten as Eq.6.

$$\eta_{STF} = \frac{E^0_{CO_2RR} \cdot FE_{CO_2RR} \cdot J_{solar}}{P_{solar}} \cdot 100\% \quad \text{Eq. (S6)}$$

Eq.6 is the one used in our manuscript and other references as well[1]. We have discussed the equation in detail in our paper ($E^{0}_{CO_2RR}$ is the standard equilibrium potential for CO_2 to CO (1.34 V), FE_{CO_2RR} is the Faradaic efficiency of the CO_2RR, J_{solar} is the operating current density of photovoltaic device and P_{solar} is the incident solar power (100 mW•cm^{-2})).

Solar-driven CO_2 reduction in flow cell

Solar driven CO_2 reduction experiments was carried out in a flow cell which was similar as electrochemical reduction of CO_2 in flow cell. 1 M KOH was used as anolyte and catholyte, respectively. A 0.5 cm^2 NiFe/NF capsulated by epoxy was used as anode, while a 1.0 cm^2 *npm*-Ag was used as cathode. The electrolytic cell was powered by a commercial GaInP/GaInAs/Ge solar cell (with an effective area 0.946 cm^2), illuminated with a standard simulated AM 1.5G spectrum at 1 sun intensity from an AAA solar simulator (Enli Technology Co., Ltd.). During the operation, cell potential, current density and gas product were monitored. The sum of the Faradaic efficiencies of carbon monoxide and hydrogen is normalized to 100% due to some data points slightly exceeding 100%.

Calculation of saturation situations for three different porous structures:

The relationship between critical pore size (L_c) and critical burst-through pressure (ΔP) follows the equation

$$L_c = -\frac{\sigma \times \cos(\theta_a)}{\Delta P} \quad \text{(Eq. S7)}$$

Where, σ is the surface tension of 1 M KOH solution (74 $mN \cdot cm^{-2}$), and θ_a is the average advancing contact angle measured for one drop of 1 M KOH solution on a smooth Ag film (89°).

The abundance of three-phase interfaces in the catalyst layer is qualitatively described by volume fraction of wetted pores, *i.e.* saturation, which depends on pore size distribution. For simplification, it is assumed that the volume fraction of pores (V_L/V_{total}) should satisfy normal distribution

$$\frac{V_L}{V_{total}} = \frac{1}{SD \times \sqrt{2\pi}} \times \exp[-\frac{(L - L_{mean})^2}{2 \times SD^2}] \quad \text{(Eq. S8)}$$

Where, L_{mean} and SD are the mean pore size and standard deviation in the pore size distribution respectively. Under a certain pressure, pores smaller than the corresponding critical size should be fully wetted. Thus, the integral of each pore size distribution curve at the critical size represents corresponding saturation.

$$\text{Saturation}(\Delta P) = \int_0^{L_c} \frac{V_L}{V_{total}} \times dL \quad \text{(Eq. S9)}$$

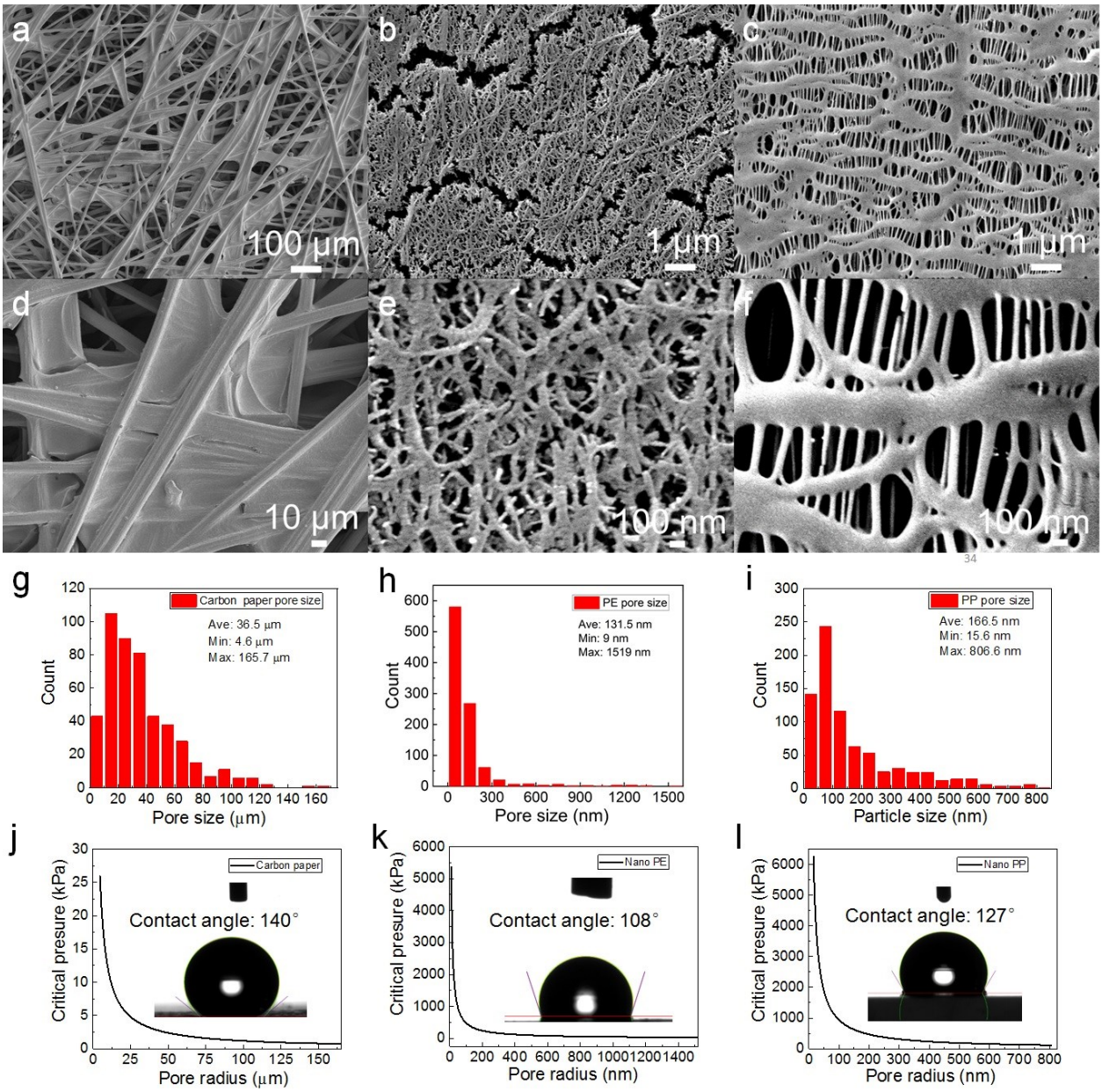

Figure. S1 | SEM images, statistics of aperture distribution and anti-flooding properties for three types of gas-permeable substrates. (**a**), (**d**), (**g**) and (**j**) Toray PTFE treated Carbon Paper (Toray, TGP-H-60); (**b**), (**e**), (**h**) and (**k**) for nano-polyethylene membranes (*nano*PE); and (**c**), (**f**), (**i**) and (**l**) for nano-polypropylene membranes (*nano*PP). Based on Eq. S1, the critical burst-through pressure is inversely proportional to the pore size. The average diameter of the pores in carbon paper (36.5 μm) and the largest pore (165.7 μm) are much larger than the pores in the PE membranes (average: 166.5 nm, largest: 1.52 μm) and PP membranes (average: 131.5 nm, largest: 806.6 nm). Thus, carbon paper based gas diffusion electrode should be more easily flooded than *nano*PE and *nano*PP. Compared to *nano*PE, *nano*PP appears a more attractive substrate for gas-diffusion electrodes than *nano*PE because the former has more uniform pore morphology, stronger hydrophobicity, and higher heat-resistance temperature.

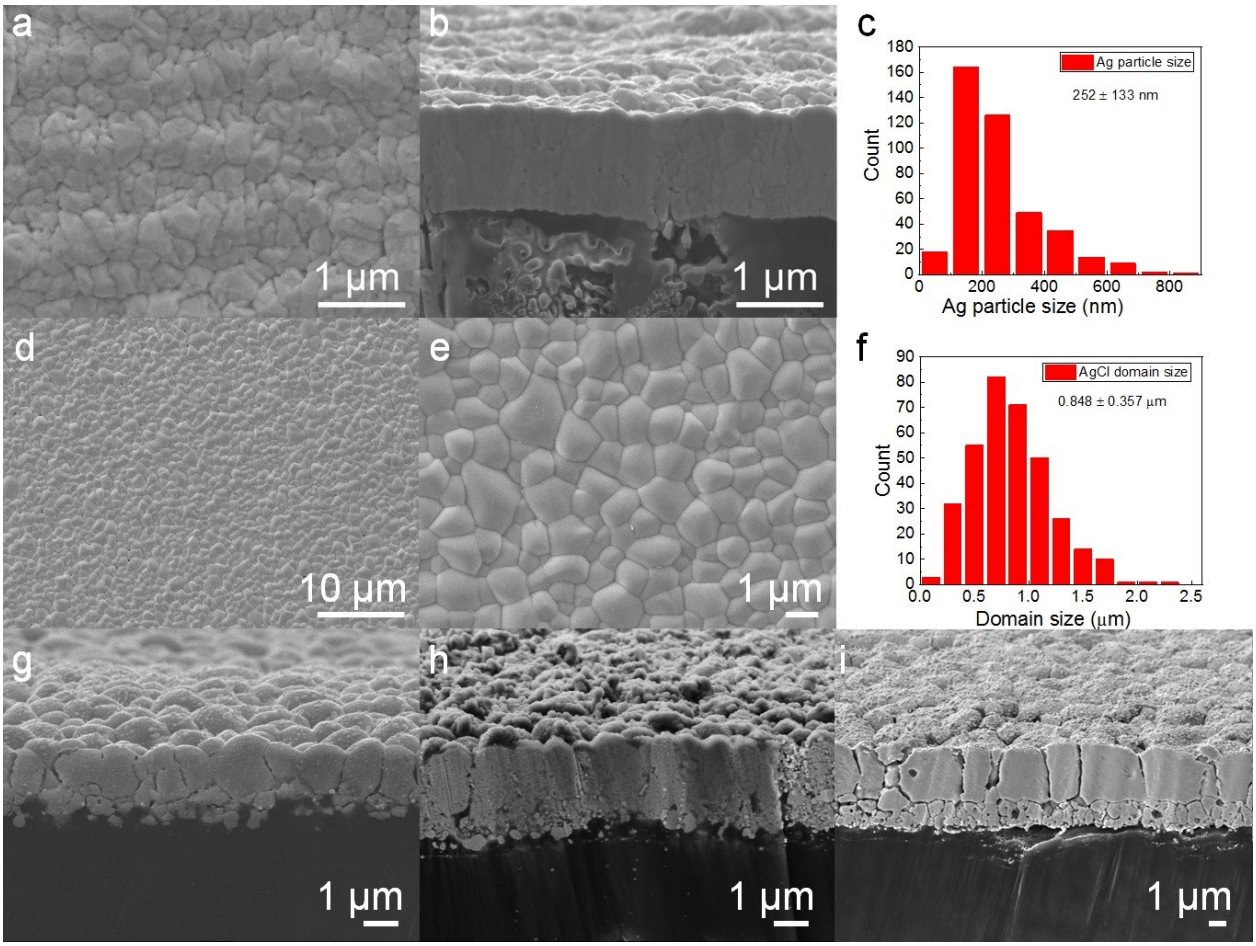

Figure. S2 | Morphology characterization of deposited Ag and anodized AgCl films on *nano*PP. (**a**) A plane-view and (**b**) cross-section view SEM image of deposited Ag film; (**c**) Size distribution diagram of Ag particles based on SEM image; (**d**) A plane-view, (**e**) high-resolution SEM image of AgCl film; (**f**) size distribution diagram of AgCl domain based on SEM image; Cross-section SEM image of AgCl film with different thickness (**g**) *ca.* 1.44 μm, (**h**) *ca.* 2.80 μm, and (**i**) *ca.* 4.50 μm, respectively.

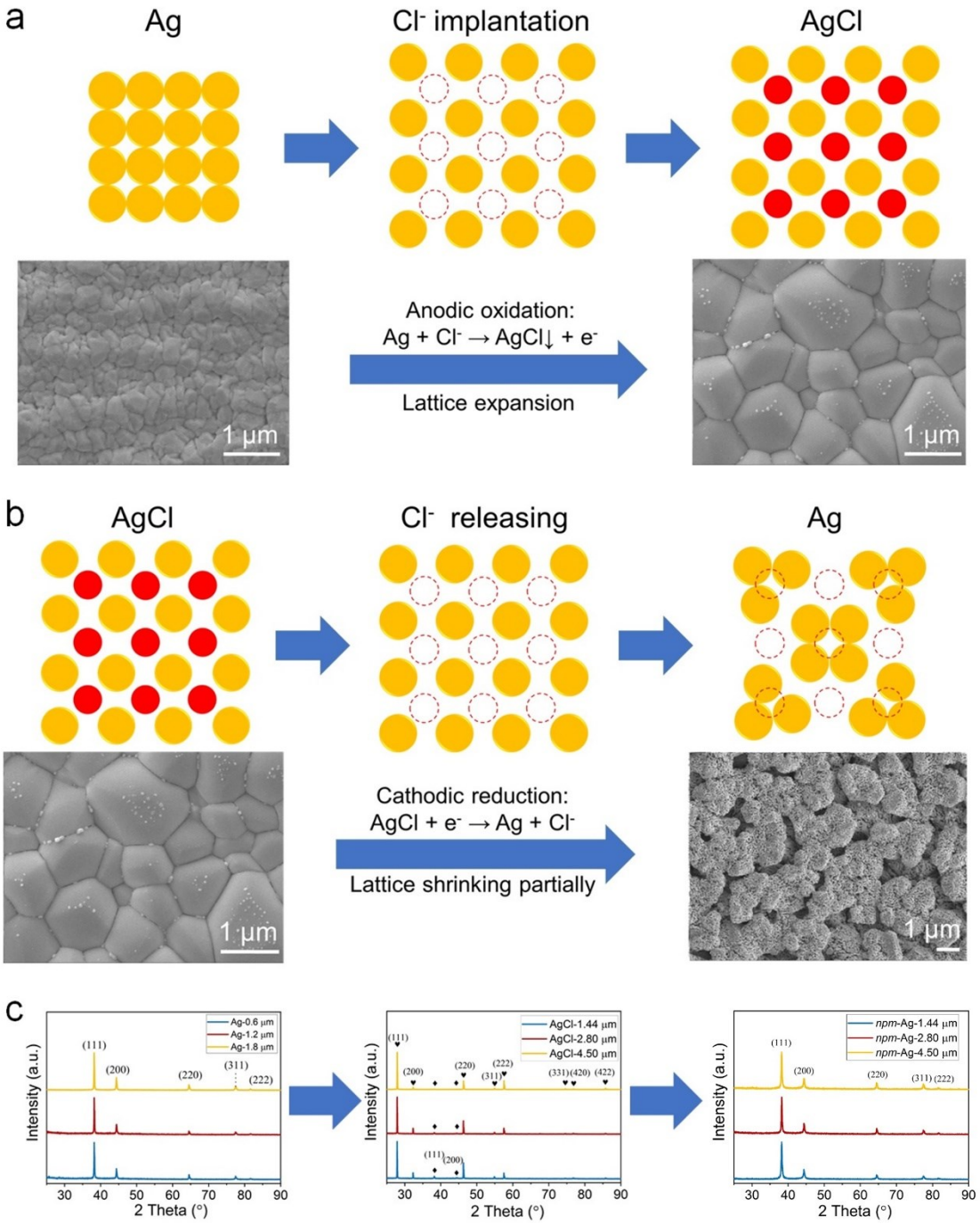

Figure. S3 | Illustration of lattice expansion and shrinkage strategy for the synthesis of *npm*-Ag and corresponding XRD diffraction patterns. (**a**) Anodic oxidation of the Ag films in aqueous HCl converted the Ag nanoparticles to AgCl micron domains through Cl^- implanting into Ag lattice, which led to a lattice expansion; and (**b**) cathodic reduction removed chloride from the AgCl lattice, leading to the formation of abundant large channels/gaps at domain boundaries and small pores in the domains due to lattice shrinkage and chloride loss; (**c**) XRD diffraction patterns show the crystal phase transformation among original Ag films, AgCl films, and *npm*-Ag films.

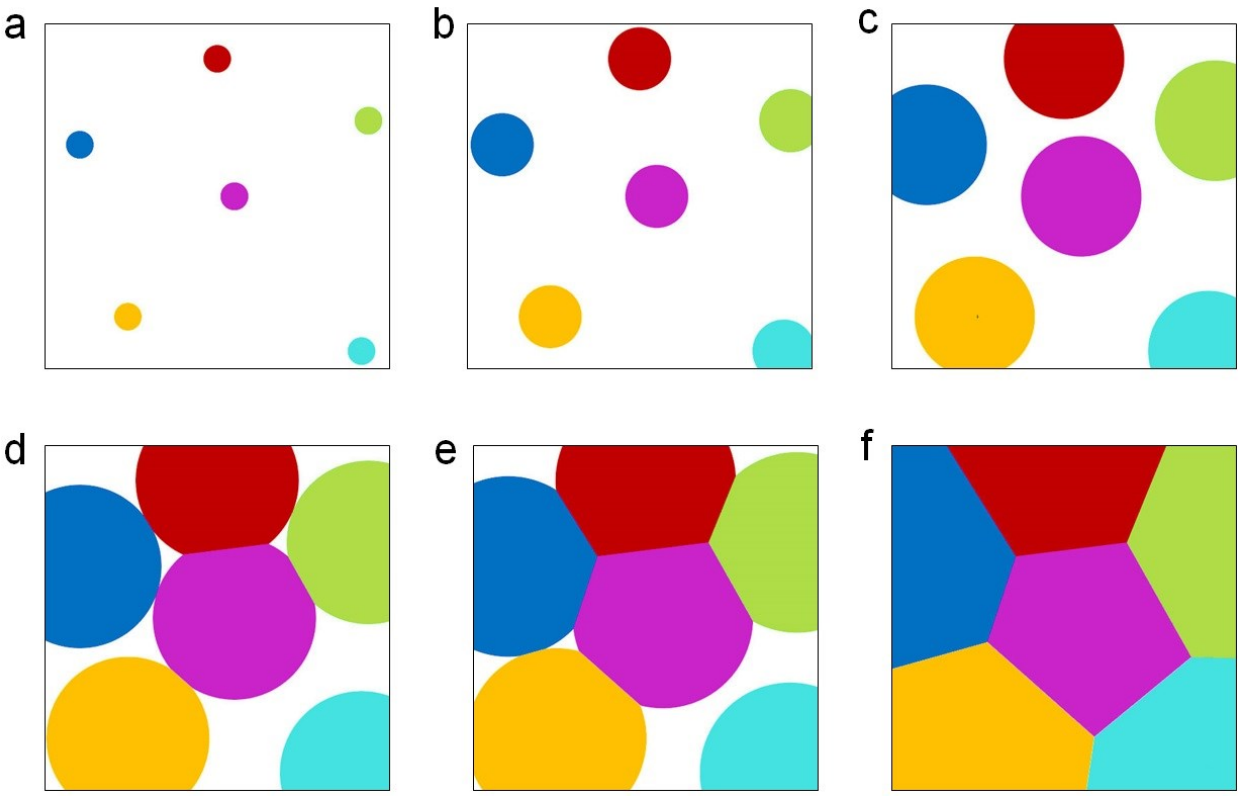

Figure. S4 | Matlab-generated Voronoi diagram for different stages in the AgCl domain growing process. Five dots were randomly created to describe the random formation of AgCl crystal seeds. According to the Voronoi model, the seeds then grew isotropically with equal speeds. The domains grew continuously until all space was occupied. The boundaries were formed once two adjacent AgCl domains encounter each other.

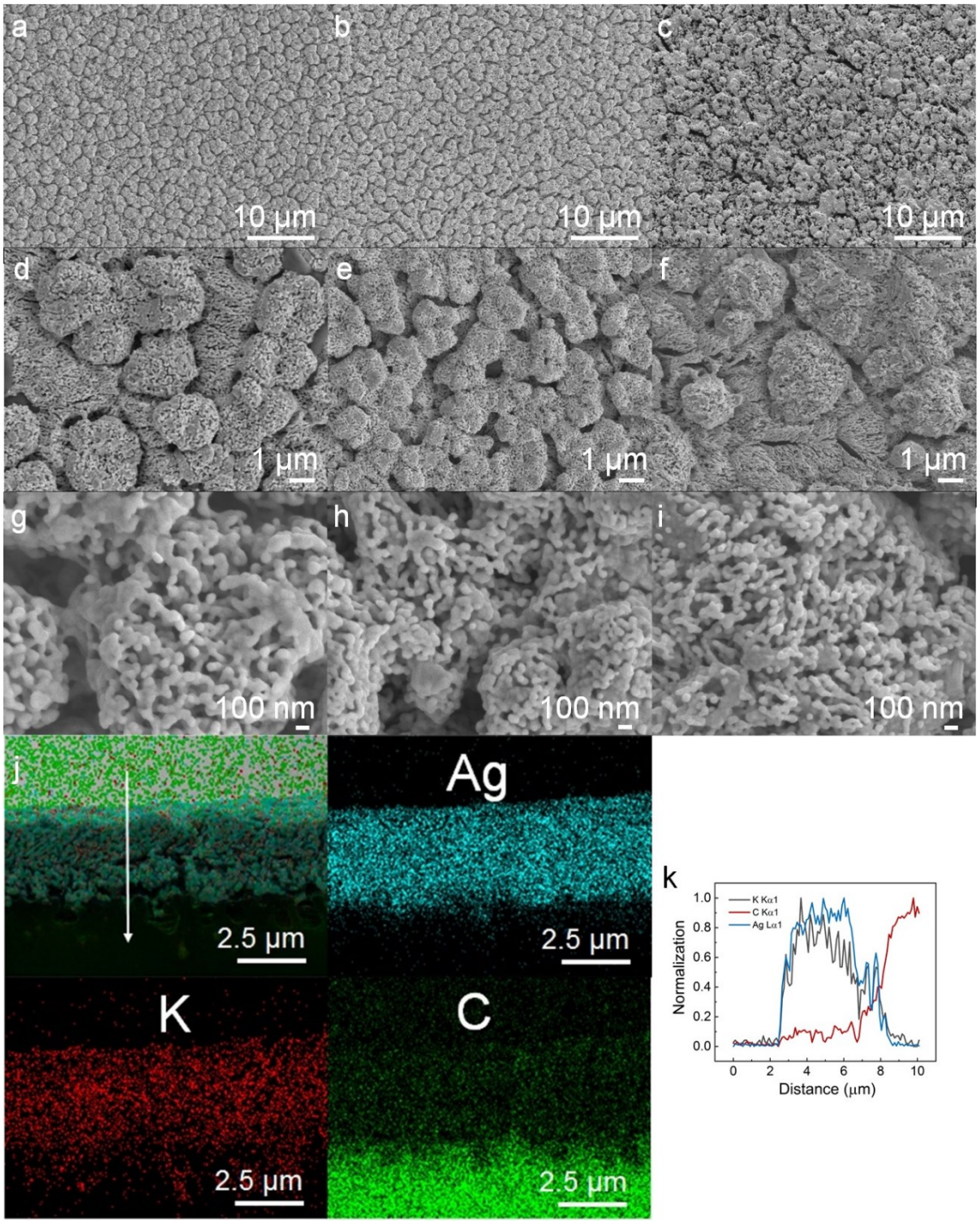

Figure. S5 | Morphology and composition characterization of *npm*-Ag. (**a**), (**d**) and (**g**) *npm*-Ag-1.44 μm; (**b**), (**e**) and (**h**) *npm*-Ag-2.80 μm; (**c**), (**f**) and (**i**) *npm*-Ag-4.50 μm; (**j**) Cross-section view of *npm*-Ag-2.80 μm and EDS elemental mapping of Ag (blue), (E) K (red), and C (green); (**k**) EDS line-scanning of elements (K, C, Ag) amount distribution along the arrow line across the profile of *npm*-Ag-2.80 μm.

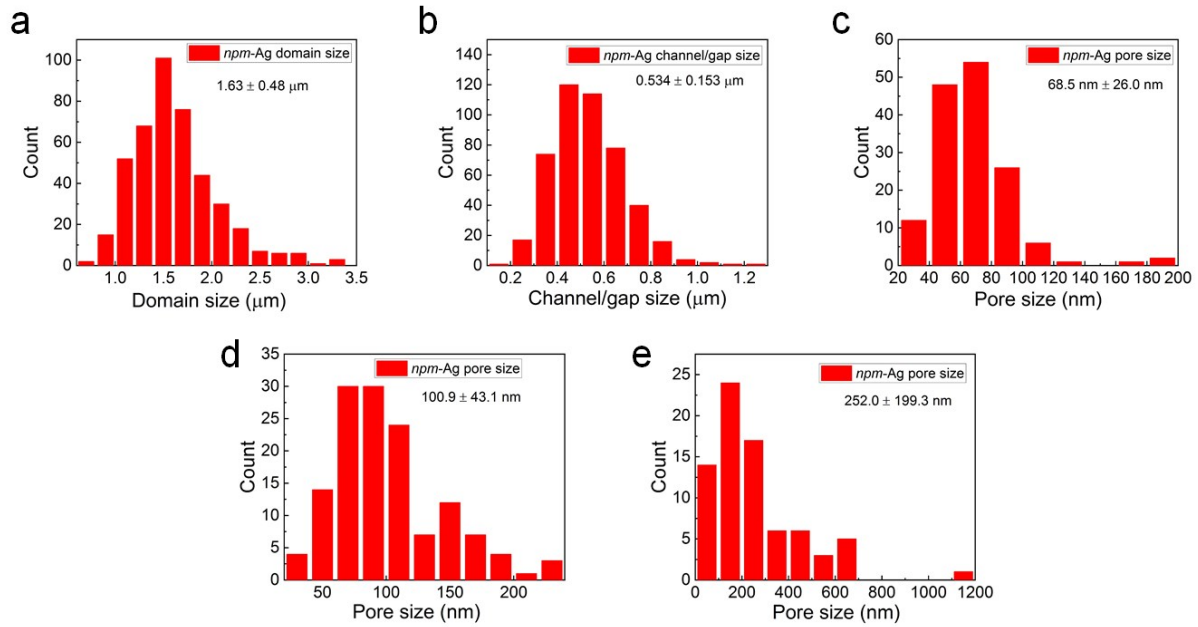

Figure. S6 | Morphology statistical distribution of *npm*-Ag-2.80 μm. Size distribution of domain (**a**), large channel/gap (**b**) and small nanopore (**c**); Pore size distribution analysis for the top (**d**) and the bottom (**e**) of *npm*-Ag-2.80 μm.

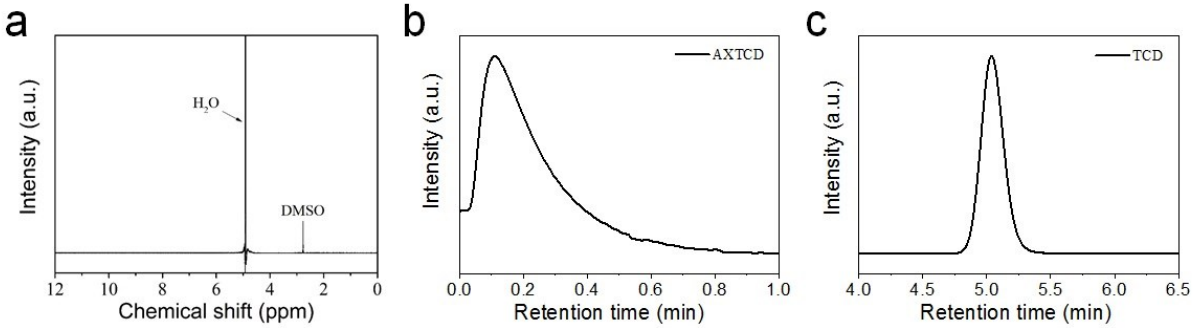

Figure. S7 | CO_2RR production analysis. (**a**) A representative ^{1}H-NMR spectrum of the electrolyte after the test of *npm*-Ag-2.80 μm at selected applied potential. DMSO was added as inner standard. The GC chromatography of H_2 (**b**) and CO (**c**). The retention times were compared with authentic samples. The retention times of H_2 and CO were *ca.* 0.88 min and *ca.* 5.08 min.

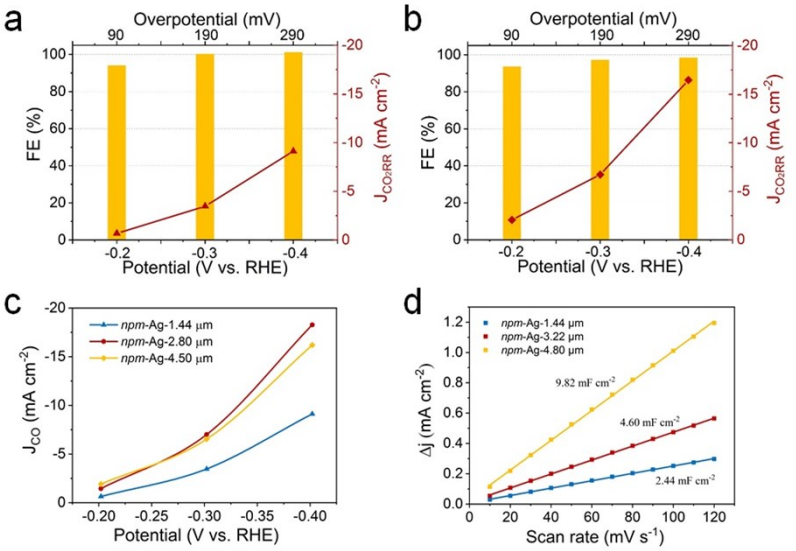

Figure. S8 | Electrochemical performance of *npm*-Ag electrodes. (**a**) Faradaic efficiency of CO and total current density for *npm*-Ag-1.44 μm; (**b**) Faradaic efficiency of CO and total current density for *npm*-Ag-4.50 μm; (**c**) The partial current density of CO for all three electrodes; (**d**) Electrochemical surface area (ECSA) tests. Double-layer charging via CVs was measured in the potential range with no apparent Faradaic process. The differences of current densities between anodic and cathodic scans with the different scan rates were fitted linearly to determine the double layer capacitance (C_{dl}) and electrochemical surface area (ECSA). The C_{dl} (2.44 mF cm^{-2}, 4.60 mF cm^{-2}, 9.82 mF cm^{-2}) and ECSA (392.8 cm^2, 184.0 cm^2, 97.6 cm^2) were measured for *npm*-Ag-1.44/2.80/4.50 μm, respectively.

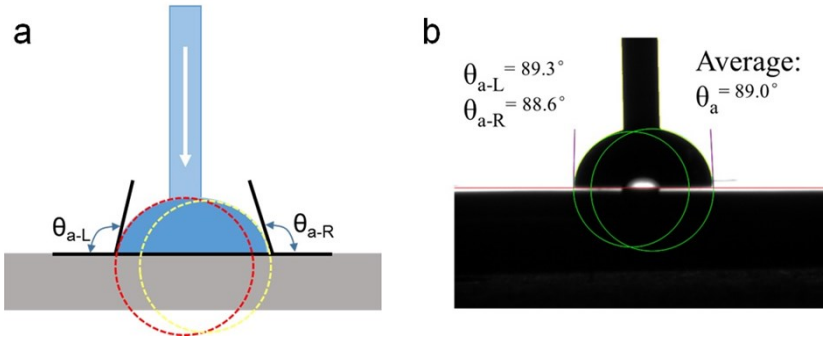

Figure. S9 | Advancing contact angle measurement. (**a**) Schematic and (**b**) measurement of the advancing contact angle of 1 M KOH solution on a smooth Ag/*nano*PP surface using a double circle tangent method.

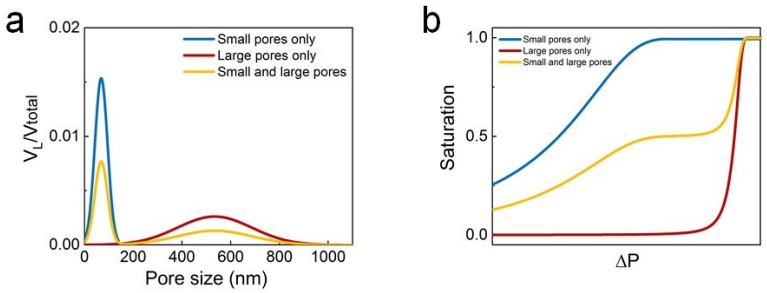

Figure. S10 | Saturation of the hierarchical pore structures in the catalyst layer. Pore size distributions with mean diameter of 68.5 ± 26.0 nm and 534 ± 153 nm were constructed to represent the small pores only and large pores only conditions respectively. The volume fraction of small and large pores were set as the same in the bimodal distribution to specifically investigate the impact of co-existence of hierarchical nanopores (a). The saturation as a function of pressure for various pore size distribution (b).

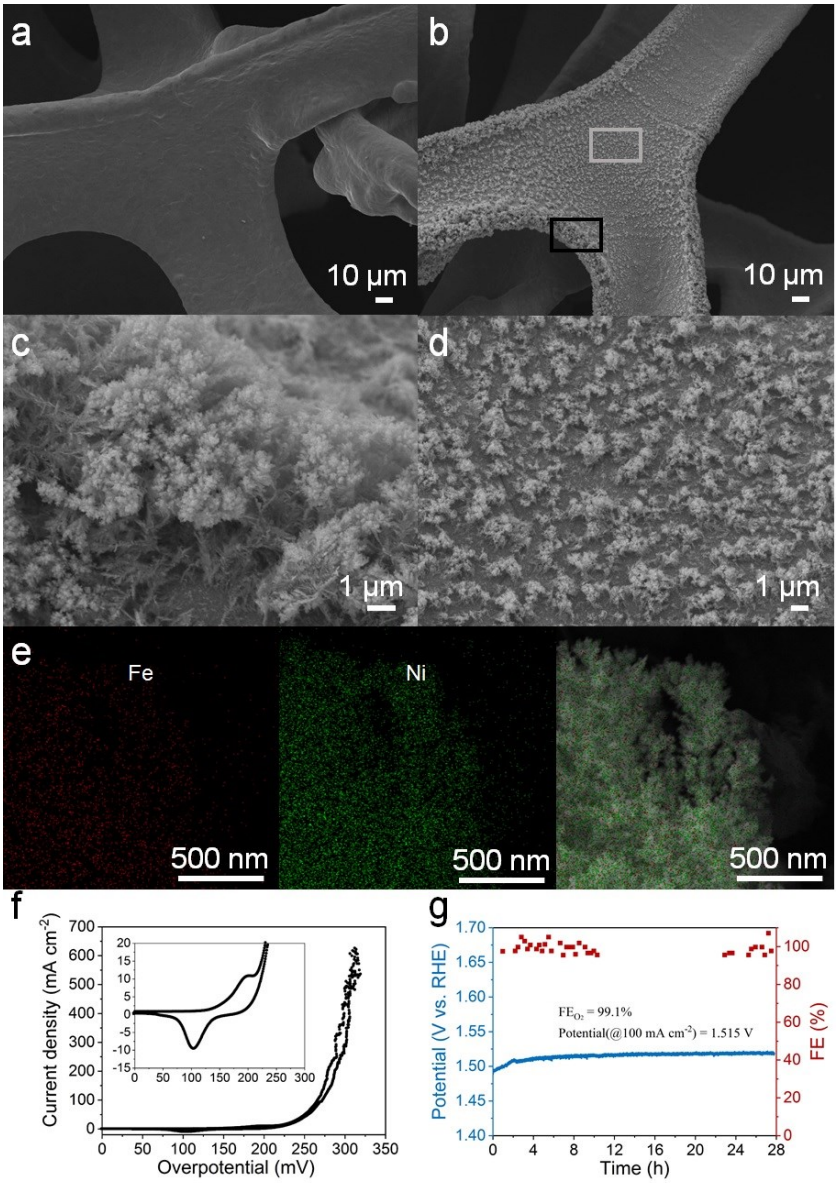

Figure. S11 | Characterization and electrochemical performance of the NiFe-based catalysts. SEM images of the as-received NF (**a**) and the as-prepared NiFe/NF (**b**). Magnified view of the black rectangular region (**c**) and the gray rectangular region (**d**) in (**b**). FESEM images showed that forest-like NiFe-based catalyst directly grow on the NF. (**e**) Scanning electron microscopy energy-dispersive X-ray spectroscopy (SEM-EDS) of the NiFe-based catalysts peeled off from the NF substrate: EDS elemental maps of Fe (red) and Ni (green) and their overlay with SEM image; (**f**) Cyclic voltammetry curves of the NiFe-based catalyst for OER with 5mV s^{-1} scan rate in 1M KOH. (g) The stability tests were performed in 1M KOH by chronopotentiometric measurements at 100 $mAcm^{-2}$, and the average Faradaic efficiency of oxygen was measured as 99.1% by a drainage method.

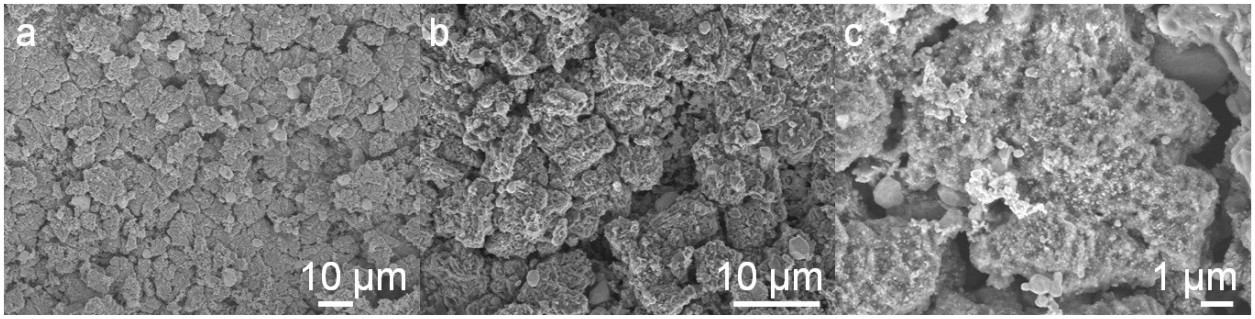

Figure. S12 | Morphology characterization of *npm*-Ag-2.80 μm after long-term electrolysis. (a), (b) and (c) are SEM images with different magnifications for *npm*-Ag-2.80 μm.

Table S1 | Parameter comparison of commercial solar cells.

Solar cell	V_{OC} (V)	J_{SC} (mA cm^{-2})	FE (%)	η_{solar} (%)	Ref.
c-Si	0.744	42.3	83.8	26.3	[2]
p-Si	0.684	41.5	82.2	23.3	[3]
a-Si	0.896	16.36	69.8	10.2	[4]
CIGS	0.734	39.58	80.4	23.35	[5]
CZTS	0.731	21.74	69.27	11.01	[6]
CZTSSe	0.513	35.21	69.8	12.6	[7]
CdTe	0.887	31.69	78.5	22.1	[5]
Dye	0.744	22.47	71.2	11.9	[5]
Organic	0.84	20.5	75	12.9	[8]
Perovskite	1.195	24.16	84	24.2	[9]
InP	0.939	31.16	82.6	24.2	[10]
GaAs	1.107	29.6	84.1	27.6	[11]
GaInP	1.470	16.63	90.2	22.0	[5]
GaAsP/Si	1.673	14.94	80.3	20.1%	[5]
GaInAsP/GaInAs	2.024	19.51	82.5	32.6	[12]
GaInP/GaAs	2.568	14.56	87.7	32.8	[5]
GaInP/GaInAs/Ge	2.54	17.52	85.2	37.9	[1c]
GaInP/GaAs/GaInAs	3.013	14.60	85.8	37.8	[5]
InGaP/GaAs/InGaAs	3.065	14.27	86.7	37.9	[5]
GaInP/GaAs/Si	3.127	12.7	83.8	33.3	[13]
4-jun-Ⅲ-Ⅴ cell (1.88/1.42/1.12/0.74 ev)	3.302	12.42	84.1	34.5 (AM1.5d)	[14]
5-jun-Ⅲ-Ⅴ cell (2.2/1.7/1.4/1.05/0.73 ev)	4.76	9.41	84.4	37.8	[15]
6-jun-Ⅲ-Ⅴ cell (2.1/1.7/1.4/1.13/0.91/0.70 ev)	5.549	8.46	83.5	39.2	[16]

Here, V_{OC} means the open circuit voltage of one solar cell, J_{SC} means the short circuit current density of a solar cell, η_{solar} means the solar energy conversion efficiency of a solar cell.

Table S2 | Attribution of potential contributions of a desirable photosynthetic system.

Potential distribution	**Potential (mV) at 15.2 mA cm^{-2}**
Photosynthetic system operating voltage	*ca.* 2200
E^0_{CO2RR}	1340
Total working overpotential	*ca.* 860
Ohmic loss (electrolyte + membrane)	*ca.* 250
Overpotential from reaction electrodes (cathode + anode)	*ca.* 600
Cathode overpotential	*ca.* 300
Anode overpotential	*ca.* 300

To construct a photosynthetic system with high solar-to-fuel conversion efficiency, the system operating voltage from the commercial solar cell should not be greater than *ca.* 2.2 V. Based on the simulation of potential distribution in an aqueous GDE cell system[17], the ohmic loss is estimated to be *ca.* 250 mV for electrolyte and membrane ohmic loss. Thus, the total overpotential for cathode and anode should not be greater than *ca.* 600 mV, giving a *ca.* 300 mV overpotential for CO_2RR and OER, respectively.

Table S3 | Lattice parameters of AgCl and Ag

	AgCl	**Ag**
a	5.47 Å	4.086 Å
b	5.47 Å	4.086 Å
c	5.47 Å	4.086 Å
α	90°	90°
β	90°	90°
γ	90°	90°
Cell volume	163.667 $Å^3$	68.2 $Å^3$

$$\frac{V_{AgCl}}{V_{Ag}} = \frac{163.667 Å^3}{68.2 Å^3} = 2.40$$

Table S4 | Stability test for the solar-to-fuel efficiency of the present system.

Time (h)	FE_{H2} (%)	FE_{CO} (%)	J_{solar} (mA cm^{-2})	Votage (V)	η_{STF} (%)
0.31	0.10	99.90	14.94	2.132	20.00
1.25	0.07	99.93	15.23	2.129	20.39
2.69	0.09	99.91	15.19	2.127	20.34
3.61	0.16	99.84	15.18	2.133	20.31
4.58	0.13	99.87	15.16	2.143	20.28
5.61	0.38	99.62	15.12	2.15	20.19
6.47	0.63	99.37	15.09	2.149	20.09
7.03	0.30	99.70	15.10	2.155	20.17
7.69	0.68	99.32	15.07	2.16	20.06
8.14	0.69	99.31	15.38	2.168	20.47
15.44	1.38	98.62	14.98	2.199	19.80
16.48	1.74	98.26	15.02	2.22	19.78
24.39	1.63	98.37	14.91	2.31	19.65
26.64	0.19	99.81	15.14	2.25	20.24
27.70	0.26	99.74	15.12	2.27	20.21

Calculation of CO concentration in the output gas during CO_2RR at high current density:
The experimental parameters are following below: S=1 cm^2, J_{CO}=100 mA·cm^{-2}, FE_{CO}=100%,

$$V_{CO} = \frac{J_{CO} \times S \times 60s \times 22.4L/mol}{96485 \times z} = 0.6965mL$$

v_{CO2}=20 sccm, z=2; and the dissolution of CO_2 in alkaline electrolyte is not considered. The volume of CO generated in 1 min is

And the concentration of CO in the output gas is

$$\frac{v_{CO}}{v_{CO2}} = \frac{0.6965}{20 - 0.6965} = 3.6\%$$

When powered by solar cells, relatively low solar current density set limit to the concentration of CO in the output gas while when operated separately under higher current density, higher concentration of CO was measured. In both cases, CO_2 was the dominant gas species even with the continuous consumption by alkaline electrolyte which is unavoidable and also observed in the neutral electrolyte due to extremely high pH in the local catalytic environment[18].

Table S5. Comparison of the present system with previous photosynthetic systems.

Anode	Cathode	J_{ap} (mA cm^{-2})	E_{ca} (V vs. RHE)	Production	FE (%)	System voltage (V)	V_{OC} (V)	J_{SC} (mA cm^{-2})	Solar cell	η_{solar} (%)	η_{STF} (%)	Stability (h)	Year	Ref.
IrO_2	Porous-Au	5.8	-0.4	CO	90	2.0	3.1	6.15	Perovskite	13.4	6.5	18	2015	[19]
Iridium oxide	Indium foil	-	*ca.* -2.1	Formate	67.1	3.85	-	-	poly-Si panel	8.7	1.8	1.5	2014	[20]
IrO_x	p-RuCP	3.3	-0.24	Formate	94	2.1	*ca.0.6*	*ca.* 4.4	SiGe-jn	7.7	4.6	6	2015	[21]
CoPi	Co-P	-	-	Biomass	-	2.2	-	-	Si	18	9.7	-	2016	[22]
Ir-CCM	np-Ag	6.26	-	CO	78.1	2.77	*2.9*	*31.28*	Si module	19.7	6.5	0.5	2017	[23]
IrO_x	Ag-GDE	48.2	-	Acetate, ethanol (fermentation)	100	3.7	-	-	Si module	11	8	-	2018	[24]
Ni	Pd/C	8.5	-	Formate	94	2.04	2.4	8.5	GaAs/InGaP/TiO_2/	-	10	6	2016	[25]
CoPi	CoP	-	-	Biomass	-	2.3	2.44	12.7	$GaInP_2$/GaAs/ Ge	21.2	6.2	24	2017	[26]
Co_3O_4 NPs	NiN-GS	5	-0.82	CO	93.2	2.34	2.5	6.7	$GaInP_2$/GaAs/Ge	27.2	12.7	20	2017	[1b]
CuO-SnO_2	CuO-SnO_2	0.4	-0.6	CO	97	2.38	2.54	13.5	GaInP/GaInAs/Ge	28.5	13.4	5	2017	[1a]
NiFe$(OH)_x$	Nano-Au	>6.0	-0.57	CO	92	1.96	2.54	17.52	InGaP/GaAs/Ge	37.9	16.4	24	2018	[1c]
Ir/C	mpBi	3.3	-	Formate	-	2.5	2.58	9.6	GaInP/GaInAs/Ge	-	1.5	3	2018	[27]
NiFe lO	Au25	40	-0.29	CO	95	1.63			$Ga_{0.5}In_{0.5}P$/GaAs	29.3%	18	12	2019	[28]
NiFe/Ni foam	Ag/PP	14.4	-0.3	CO	100	2.12	2.67	15.4	GaInP/GaInAs/Ge	32	**20.4**	28	2020	**Our work**

Here, J_{ap} means the applied current density, E_{ca} means the cathode potential, FE means the Faradaic efficiency of the cathode for CO_2RR, V_{OC} means the open circuit voltage of one solar cell, J_{SC} means the short circuit current density of a solar cell, η_{solar} means the solar energy conversion efficiency of a solar cell, and η_{STF} means the CO_2-reducing solar-to-fuel efficiency.

References

[1] a) M. Schreier, F. Heroguel, L. Steier, S. Ahmad, J. S. Luterbacher, M. T. Mayer, J. S. Luo, M. Grätzel, *Nature Energy* **2017**, 2, 17087; b) K. Jiang, S. Siahrostami, A. J. Akey, Y. Li, Z. Lu, J. Lattimer, Y. Hu, C. Stokes, M. Gangishetty, G. Chen, Y. Zhou, W. Hill, W.-B. Cai, D. Bell, K. Chan, J. K. Nørskov, Y. Cui, H. Wang, *Chem* **2017**, 3, 950; c) Y. Wang, J. Liu, Y. Wang, Y. Wang, G. Zheng, *Nat Commun* **2018**, 9, 5003.

[2] K. Yoshikawa, H. Kawasaki, W. Yoshida, T. Irie, K. Konishi, K. Nakano, T. Uto, D. Adachi, M. Kanematsu, H. Uzu, K. Yamamoto, *Nat Energy* **2017**, 2, 17032

[3] J. Benick, A. Richter, R. Muller, H. Hauser, F. Feldmann, P. Krenckel, S. Riepe, F. Schindler, M. C. Schubert, M. Hermle, A. W. Bett, S. W. Glunz, *Ieee J Photovolt* **2017**, 7, 1171.

[4] T. Matsui, A. Bidiville, K. Maejima, H. Sai, T. Koida, T. Suezaki, M. Matsumoto, K. Saito, I. Yoshida, M. Kondo, *Applied Physics Letters* **2015**, 106, 053901

[5] M. A. Green, E. D. Dunlop, D. H. Levi, J. Hohl-Ebinger, M. Yoshita, A. W. Y. Ho-Baillie, *Prog. Photovoltaics* **2019**, 27, 565.

[6] C. Yan, J. Huang, K. Sun, S. Johnston, Y. Zhang, H. Sun, A. Pu, M. He, F. Liu, K. Eder, L. Yang, J. M. Cairney, N. J. Ekins-Daukes, Z. Hameiri, J. A. Stride, S. Chen, M. A. Green, X. Hao, *Nat Energy* **2018**, 3, 764.

[7] W. Wang, M. T. Winkler, O. Gunawan, T. Gokmen, T. K. Todorov, Y. Zhu, D. B. Mitzi, *Advanced Energy Materials* **2014**, 4, 1301465.

[8] S. Dong, K. Zhang, B. Xie, J. Xiao, H.-L. Yip, H. Yan, F. Huang, Y. Cao, *Advanced Energy Materials* **2019**, 9, 1802832.

[9] E. H. Jung, N. J. Jeon, E. Y. Park, C. S. Moon, T. J. Shin, T.-Y. Yang, J. H. Noh, J. Seo, *Nature* **2019**, 567, 511.

[10] M. Wanlass *Unitied States Patent US 9,590,131 B2*, **2017**.

[11] B. M. Kayes, H. Nie, R. Twist, S. G. Spruytte, F. Reinhardt, I. C. Kizilyalli, G. S. Higashi, in *2011 37th IEEE Photovoltaic Specialists Conference*, DOI: 10.1109/PVSC.2011.6185831, Seattle, WA 2011, 000004.

[12] N. Jain, K. L. Schulte, J. F. Geisz, D. J. Friedman, R. M. France, E. E. Perl, A. G. Norman, H. L. Guthrey, M. A. Steiner, *Applied Physics Letters* **2018**, 112, 053905

[13] R. Cariou, J. Benick, F. Feldmann, O. Hohn, H. Hauser, P. Beutel, N. Razek, M. Wimplinger, B. Blasi, D. Lackner, M. Hermle, G. Siefer, S. W. Glunz, A. W. Bett, F. Dimroth, *Nat Energy* **2018**, 3, 326.

[14] F. Dimroth, M. Grave, P. Beutel, U. Fiedeler, C. Karcher, T. N. D. Tibbits, E. Oliva, G. Siefer, M. Schachtner, A. Wekkeli, A. W. Bett, R. Krause, M. Piccin, N. Blanc, C. Drazek, E. Guiot, B. Ghyselen, T. Salvetat, A. Tauzin, T. Signamarcheix, A. Dobrich, T. Hannappel, K. Schwarzburg, *Progress in Photovoltaics: Research and Applications* **2014**, 22, 277.

[15] P. T. Chiu, D. C. Law, R. L. Woo, S. B. Singer, D. Bhusari, W. D. Hong, A. Zakaria, J. Boisvert, S. Mesropian, R. R. King, N. H. Karam, *Ieee J Photovolt* **2014**, 4, 493.

[16] J. F. Geisz, M. A. Steiner, N. Jain, K. L. Schulte, R. M. France, W. E. McMahon, E. E. Perl, D. J. Friedman, *Ieee J Photovolt* **2018**, 8, 626.

[17] L.-C. Weng, A. T. Bell, A. Z. Weber, *Energy & Environmental Science* **2019**, 12, 1950.

[18] F. Li, A. Thevenon, A. Rosas-Hernández, Z. Wang, Y. Li, C. M. Gabardo, A. Ozden, C. T. Dinh, J. Li, Y. Wang, J. P. Edwards, Y. Xu, C. McCallum, L. Tao, Z.-Q. Liang, M. Luo, X. Wang, H. Li, C. P. O'Brien, C.-S. Tan, D.-H. Nam, R. Quintero-Bermudez, T.-T. Zhuang, Y. C. Li, Z. Han, R. D. Britt, D. Sinton, T. Agapie, J. C. Peters, E. H. Sargent, *Nature* **2020**, 577, 509.

[19] M. Schreier, L. Curvat, F. Giordano, L. Steier, A. Abate, S. M. Zakeeruddin, J. Luo, M. T. Mayer, M. Gratzel, *Nat Commun* **2015**, 6, 7326.

[20] J. L. White, J. T. Herb, J. J. Kaczur, P. W. Majsztrik, A. B. Bocarsly, *J. CO2 Util.* **2014**, 7, 1.
[21] T. Arai, S. Sato, T. Morikawa, *Energy & Environmental Science* **2015**, 8, 1998.
[22] C. Liu, B. C. Colón, M. Ziesack, P. A. Silver, D. G. Nocera, *Science* **2016**, 352, 1210.
[23] G. M. Sriramagiri, N. Ahmed, W. Luc, K. D. Dobson, S. S. Hegedus, F. Jiao, *Acs Sustainable Chemistry & Engineering* **2017**, 5, 10959.
[24] T. Haas, R. Krause, R. Weber, M. Demler, G. Schmid, *Nature Catalysis* **2018**, 1, 32.
[25] X. Zhou, R. Liu, K. Sun, Y. Chen, E. Verlage, S. A. Francis, N. S. Lewis, C. Xiang, *ACS Energy Letters* **2016**, 1, 764.
[26] C. Liu, B. E. Colón, P. A. Silver, D. G. Nocera, *Journal of Photochemistry and Photobiology A: Chemistry* **2018**, 358, 411.
[27] H. Yang, N. Han, J. Deng, J. Wu, Y. Wang, Y. Hu, P. Ding, Y. Li, Y. Li, J. Lu, *Advanced Energy Materials* **2018**, 8, 1801536.
[28] B. Kim, H. Seong, J. T. Song, K. Kwak, H. Song, Y. C. Tan, G. Park, D. Lee, J. Oh, *ACS Energy Letters* **2020**, DOI: 10.1021/acsenergylett.9b02511749.